Journal of Alloys and Compounds 1025 (2025) 180307

Contents lists available at ScienceDirect

Journal of Alloys and Compounds

journal homepage: www.elsevier.com/locate/jalcom

Introduction of sulfur into an eutectic of the Zr-Ti-Ni-Cu system: Alloy development and characterization of the $(Zr_{50}Ti_{16.6}Ni_{18.3}Cu_{15})_{100-x}S_x$ bulk metallic glasses

Bastian Adam [a,*], Oliver Kruse [a], Lucas Matthias Ruschel [a], Nico Neuber [a], Maximillian Frey [a], Oliver Gross [b], Hao-Ran Jiang [c], Bosong Li [d], Bernd Gludovatz [d], Jamie J. Kruzic [d], Ralf Busch [a]

[a] Chair of Metallic materials (LMW), Saarland University, Campus C6.3, Saarbrücken 66123, Germany
[b] Amorphous Metal Solutions GmbH, Homburg 66424, Germany
[c] Materials Genome Institute, Shanghai University, Shanghai 200444, China
[d] School of Mechanical and Manufacturing Engineering, University of New South Wales (UNSW Sydney), Sydney, NSW 2052, Australia

ARTICLE INFO

Keywords:
Bulk metallic glasses
Glass-forming ability
Mechanical Properties
Casting
Synchrotron diffraction

ABSTRACT

The influence of sulfur additions to the quaternary $Zr_{50}Ti_{16.6}Ni_{18.3}Cu_{15}$ alloy was investigated in terms of glass forming ability, thermophysical properties and mechanical properties in high purity alloy variants as well as in industrial grade alloys. In the latter case, oxygen was found to cause only a minor reduction of glass forming ability whilst retaining good mechanical properties. Conventional powder diffraction as well as synchrotron high energy diffraction revealed that the addition of sulfur changes the primary phase that forms during casting and the glass forming properties can be enhanced by adding a specifically tailored amount of sulfur to the alloy. The resulting alloys can be tailored to either possess a large glass forming ability with a critical casting size of 6 mm with 2–3 at% S or a large supercooled liquid region for sulfur amounts above 6 at%. Mechanical properties show a compressive strength of 1.6 GPa paired with high ductility, that shows in a compressive strain to failure ≥ 5.8 %, as well as conditional fracture toughness values of $K_Q \geq 79\ MPa\sqrt{m}$ in both the high purity and industrial grade variants, despite severe oxygen contamination. This indicates superior resistance against embrittlement compared to other Zr-based bulk metallic glasses.

1. Introduction

Amorphous metals or metallic glasses are alloys that can form a glass while being rapidly quenched from the high temperature equilibrium melt rather than forming a crystalline phase upon solidification. Metallic glasses are under extensive research due to their unique properties; they can typically reach high elastic strain limits of about 2 % paired with high hardness and yield strengths, often surpassing the mechanical performance of conventional crystalline alloys [1]. Bulk metallic glasses (BMG) are compositions that can be quenched into the amorphous state in dimensions beyond 1 mm thickness [1]. Zr-based BMGs are being manufactured commercially and can be produced in casting dimensions ranging up to 1 cm, starting with the introduction of Vitreloy 1 alloy (Zr-Ti-Ni-Cu-Be) in the early 1990s [2]. In recent years, a vast number of BMGs were reported for the Zr-Cu [3], Zr-Cu-Al [4], Zr-Cu-Ni-Al [4], as well as Ti-Zr-Ni-Cu [5] and Zr-Ti-Ni-Cu-Al [6] systems followed by numerous derivatives of those systems. Explicitly the alloys Vitreloy 105 ($Zr_{52.5}Ti_5Cu_{17.9}Ni_{14.6}Al_{10}$) and AMZ4 ($Zr_{59.3}Cu_{28.8}Al_{10.4}Nb_{1.5}$) are to be mentioned due to the high commercial interest of these systems in recent research activities and their potential for industrial applications [7–9]. These alloys are used as reference materials for this study.

Zr-based BMGs have been among the more promising BMGs for mechanical applications. They typically possess a high glass forming ability paired with a high mechanical strength and can possess extraordinary plasticity among the various families of BMG [10]. Those properties make Zr-based BMGs interesting for industrial applications; however, most of the alloys' GFA as well as mechanical properties are strongly deteriorated when being produced from industrial quality metal elements with a high oxygen contamination [11,12]. This is rather unfortunate as the requirement for high purity materials increases the materials cost of BMGs and therefore significantly limits the viability of BMGs for cost-efficient applications.

* Corresponding author.
E-mail address: bastian.adam@uni-saarland.de (B. Adam).

https://doi.org/10.1016/j.jallcom.2025.180307
Received 5 February 2025; Received in revised form 4 April 2025; Accepted 7 April 2025
Available online 8 April 2025

There is a desire for newly developed BMGs that can be produced from cheaper raw materials while also being able to retain a significant GFA in Cu-mold casting. Sulfur as a constituent in BMGs was first reported in 2017 in Pd-Ni-S and Ti-Ni-S [13,14] and its beneficial glass forming effect was observed in the Ti-Zr-Ni-Cu system. The system was investigated by Kuball et al. mainly in the Ti-rich region, where a glass forming ability (GFA) of 3 mm was found for the $Ti_{40}Zr_{35}Cu_{17}S_8$ alloy and 1 mm GFA for $Zr_{56}Ti_{13.3}Ni_{13.6}Cu_{9.6}S_7$ [14,15]. These initial Ti- and Zr-based systems however were off-eutectic compositions, later works on near eutectic Ti-Cu-Ni and Ti-Zr-Cu showed a difference in behavior depending on the amount of icosahedral short-range order in the glass [16]. Since then, sulfur has been introduced into several systems, starting from further works on Ti-Zr-Ni-Cu-S [14,17] and Zr-Ti-Ni-Cu-Al-S [18] as well as Ni-Nb-S [19] to recently Cu-Zr-Al-S [20] system. This element can have a positive influence on the GFA as well as promote the stability of the supercooled liquid region (SCLR), depending on the system and the amount of sulfur addition. The amount of optimal sulfur content, in terms of GFA improvement, can vary a lot throughout the different systems and spans over a broad range from 1 at% in the Cu-Zr-Al system to 27 at% in the Pd-Ni-S system. The Zr-Ti-Ni-Cu system was intensively studied by Molokanov et al. in the compositional space of the A_2B ratio for A = (Ti, Zr) and B = (Ni, Cu). It contains multiple compositions that can be described as glass forming compositions due to the possibility to undercool the liquid before the intermetallic phases (Ti_2Ni, Zr_2Ni, Ti_2Cu, Zr_2Cu) crystallize -of which the mixtures form two eutectic points in the quaternary system [21].

This study was conducted consecutively to find the Zr-Ti-Ni-Cu-S alloy with the highest GFA and probe if the reported, beneficial properties in the Ti-Zr-Cu-S system could be reproduced [14]. Therefore, the most promising eutectic alloy from the literature in the Zr-Ti-Ni-Cu system was chosen for the systematic introduction of sulfur while keeping the ratio of the metallic elements constant. The $Zr_{50}Ti_{16.6}Ni_{18.3}Cu_{15}$ alloy was previously described by Molokanov et al. as the best glass former in the section of the stochiometric $(Zr,Ti)_2(Ni,Cu)$ system [22] and thoroughly characterized. To expand the study, industrial purity raw materials were employed in the synthesis and the glass forming ability under oxygen load was tested and cross-referenced with well-known reference alloys in industrial purity. Furthermore, the mechanical testing was expanded to fracture toughness testing and hardness mapping for comparisons between the industrial and high purity grades of the most promising developed alloy.

2. Materials and methods

2.1. Sample production

Master alloys of samples were produced in an arc melting furnace under a protective Ar atmosphere. The high purity alloys were crafted from 99.99 wt% (4 N) metallic elements and a Cu_2S pre-alloy. The pre-alloy was synthesized by encapsulating Cu and S under vacuum in a quartz capsule and heating it up to 1473 K for 4 h to ensure a homogeneous pre-alloy. For the industrial grade alloy, zirconium R60702 (Zr702 up to 1600 w-ppm oxygen according to ASTM) and titanium of commercial purity grade 2 (Ti grade 2 up to 2500 w-ppm oxygen according to ASTM) were used as alloying materials, the remaining alloy elements were 4 N pure elements. The samples were produced with compositions $(Zr_{50}Ti_{16.6}Ni_{18.3}Cu_{15})_{100-x}S_x$ ranging from x = 0 at% to 8 at % (further referred to as $Zr_{50}S_x$, x = 0, …, 8) with an increment of 1 at%. BMG-samples were produced from the master alloys by arc melting and suction casting under Ti-gettered 5 N (99.999 vol%) Ar atmosphere into water cooled copper molds. The same materials were employed and arc-melting procedure was utilized to produce reference materials of the alloys Vit105 ($Zr_{52.5}Ti_5Cu_{17.9}Ni_{14.6}Al_{10}$) and AMZ4 ($Zr_{59.3}Cu_{28.8}Al_{10.4}Nb_{1.5}$) in industrial purity grades as reference materials. The molds varied from 0.25 mm thick plates with increasing thickness up to 0.75 mm and then rod molds with diameters ranging from 2 mm up to 7 mm. Plates were used at the small dimensions since rods with a diameter below 1.5 mm could not be cast reproducibly. The fracture toughness testing samples were produced by arc melting die casting at Amorphous Metal Solutions GmbH (AMS) into 2 mm x 4 mm cross-section beams and samples were checked for porosities using X-ray tomography. The minimum pore size that could be resolved by the micro-X-ray computed tomography system was in the range of 20–30 μm.

2.2. Material characterization

Differential scanning calorimetry (DSC) experiments were performed on a PerkinElmer DSC8000 under constant 6 N Ar protective gas flux. Scan measurements were performed in Al pans with a heating rate of 20 K/min from 323 K up to 853 K. The second (crystalline) scan was subtracted from the first scan as baseline correction.

Differential thermal analysis (DTA) was performed in carbon crucibles coated with Y_2O_3 using a Netsch DSC 404 F1 Pegasus with a TG-DSC sensor using a heating rate of 20 K/min. Analysis focused on the second heating run where the previously molten sample was analyzed to obtain the characteristic temperatures of the alloy.

X-ray diffraction (XRD) patterns of the samples were recorded at room temperature on a D8-A25-Advance diffractometer (Bruker, Karlsruhe, Germany) in Bragg-Brentano θ-θ-geometry (goniometer radius 280 mm) with Cu K_α-radiation (λ = 154 pm). A 12 μm Ni foil working as K_β-filter and a variable divergence slit were mounted at the primary beam side. A LYNXEYE detector with 192 channels was used at the secondary beam side. Experiments were carried out in a 2θ range of 20° to 80° with 0.0261° per step and 500 s-per-step.

High energy synchrotron X-ray diffraction experiments (HE-XRD) were conducted at the PETRA III beamline P21.1 using a Perkin Elmer XRD1621 CsI bonded amorphous silicon detector (2048 ×2048) with a sample detector distance of 0.6 m and a radiation energy of 100 keV, corresponding to a wavelength of 0.122 Å. The acquired diffraction data was processed utilizing pyFAI [23] for azimuthal integration of the detector images and pdfGetX2 software [24] to correct the raw data appropriately and calculate the structure factor S (Q) as well as the reduced pair distribution function G(r).

The samples for 3-point beam bending (3-PBB) tests were suction cast and subsequently sanded with up to 1200 grid SiC sandpaper to ensure a smooth and reproducible surface for the bending experiments. Samples were prepared to a nominal height, *h,* of 1.8 mm and a width, *w,* of 3 mm, and tested on a Shimadzu universal testing machine with a support span, *L,* of 20 mm and at a displacement rate of 0.3 mm/min. The deflection, *D,* in the center of the sample was recorded as well as the applied force *F* that was measured with a load cell. The maximum stress σ and strain ε on the tensile surface of the beam were calculated according to Eq. (1) and Eq. (2) respectively.

$$\sigma = \frac{3FL}{2wh^2} \tag{1}$$

$$\varepsilon = \frac{6Dh}{L^2} \tag{2}$$

Vickers hardness testing was performed using a Wolpert Wilson 930 N universal hardness tester with a load of 49 N (HV5). The size of the indents was determined by an optical microscope, where 10 indentations per measurement were analyzed for statistics. Vickers microhardness maps using a load of 0.49 N (HV0.05) were measured using an automated hardness tester (Durascan 80, Struers) [25]. The minimum spacing of the indents was 40 μm. The mapped area measured 0.6 mm x 1 mm.

Single edge notched beam bending (SEN(B)) samples with a cross-section of 2 mm thickness, *B*, and 4 mm width, *W*, were used for fracture toughness testing in sets of 6 samples each for the industrial grade alloy and high purity alloy variant. The surface of each sample was

polished to a 0.1 μm surface finish. A notch with a radius of ~150 μm was cut using a diamond blade. Next, the notch tip was extended by sliding a razor blade across the diamond blade notch to create a micro-notch with a root radius of around 20 μm. Fatigue pre-cracking was performed by cycling with a 10 Hz sine wave with a ratio of minimum to maximum load of $R = P_{min}/P_{max} = 0.1$ using a computer-controlled servo-hydraulic testing machine (Model 8872, Instron Corporation, USA) with a 25 kN calibrated load cell. To initiate fatigue pre-cracks, an applied stress intensity range $\Delta K = K_{max} - K_{min}$ between 6 – 8 MPa$\sqrt{m}$ was used. Three-point bending fracture toughness tests with 16 mm loading span were conducted using an Instron 8872 dynamic test machine with a 25 kN calibrated load cell and a constant displacement rate of 1 μm/s. No samples met the sample dimensions required by ASTM E399 for valid plane strain K_{IC} measurements:

$$B, a, b \geq 2.5\left(\frac{K_Q}{\sigma}\right)^2 \tag{3}$$

$$K_J = \sqrt{\frac{E(J_{el} + J_{pl})}{1-\nu^2}} \tag{4}$$

where $b = W - a$. Accordingly, instead of K_{IC}, both K_Q and K_J fracture toughness values are reported with the latter based on the *J*-integral using Eq. (4):

In Eq. (4), J_{el} and J_{pl} are the elastic and plastic components of the *J*-integral that can be calculated by:

$$J_{el} = K_Q{}^2(1-\nu^2)/E \tag{5}$$

$$J_{pl} = \eta_{pl}A_{pl}/Bb \tag{6}$$

where $\eta_{pl} = 1.9$, A_{pl} is the area under force versus displacement curve and E and ν are Young's modulus and Poisson's ratio, respectively. The Young's modulus and Poisson's ratio were taken to be 89 GPa and 0.40, respectively.

Compression testing was performed for both high purity and industrial grade BMG samples. Compression samples with nominal dimensions of 2 × 2×4 mm^3 were cut from beams. The surfaces were ground flat and parallel prior to testing. The surfaces of the tungsten carbide loading plates were lubricated with molybdenum disulfide-based lubricant to minimize friction. The displacement rate used for the compression tests was 0.83 μm/s and a deflection gage was used to measure the displacement directly on the compression plate to calculate strain. Yield strength was determined by the 0.2 % offset strain method.

3. Results

3.1. Thermal analysis

The differential scanning calorimetry results in Fig. 1a) indicate that alloying $Zr_{50}S_0$ with S progressively increases the thermal stability of the SCLR against crystallization. The first crystallization event, associated with icosahedral phase formation, is delayed towards higher

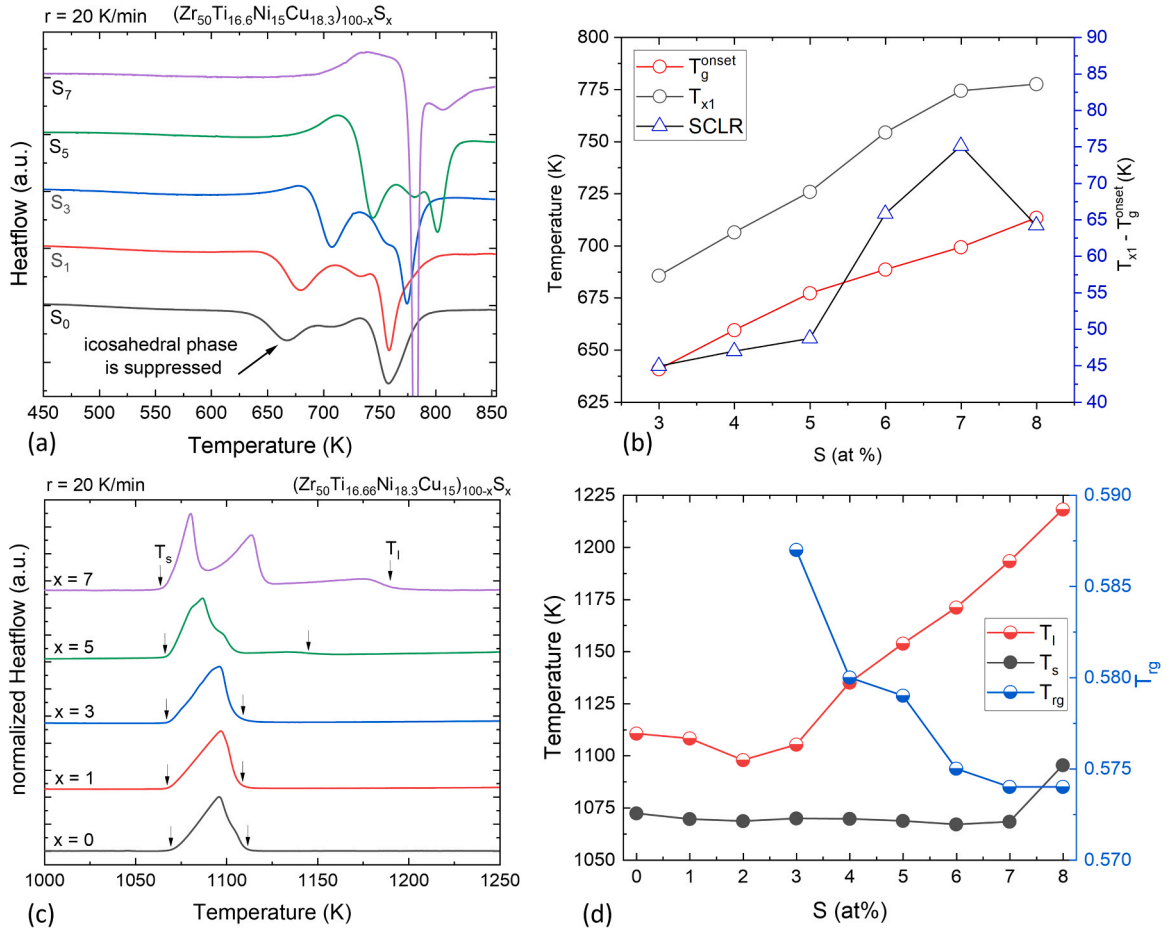

Fig. 1. a) DSC scans of the $(Zr_{50}Ti_{16.6}Cu_{15}Ni_{18.3})_{100-x}S_x$ (x = 1, 3, 5, 7) alloy series. The first icosahedral phase crystallization is continuously destabilized upon S addition, leading to a pronounced stabilization of the SCLR. b) Derived onset of the glass transition temperature T_g^{onset} and crystallization temperature T_{x1} as a function of the sulfur content. c) DTA results of the sulfur variation, showing a pronounced "melting shoulder" at higher sulfur contents. d) From the DTA measurements derived solidus temperature T_s, liquidus temperature T_l and glass formation criterion T_{rg} (T_g/T_l) as a function of the sulfur content.

temperatures T_{x1} as well as the onset of the glass transition, T_g^{onset}. Identification of an icosahedral phase as the initial crystallization phase upon devitrification was analogous to similar Ti-based systems investigated by Ruschel et al. [16] and was confirmed with in-situ diffraction data that can be seen in Figure S1. The delay in icosahedral phase formation can be observed in the comparison of T_{x1} and T_g^{onset} as a function of the sulfur content, shown in Fig. 1b). The difference in size of the SCLR can be observed quite well as the higher sulfur content leads to a significantly pronounced SCLR. The onset of the glass transition shifts 73 K from 640 K at 3 at% of sulfur towards a temperature of 713 K at 8 at% S. Below 3 at% of sulfur the SCLR is not stable enough at a scan rate of 20 K/min to determine the onset of glass transition reliable with the tangent method. The first crystallization at T_{x1} is suppressed and shifted to higher temperatures up to 754 K, which is T_{x2} of the lower proportions of sulfur containing alloys.

The solidus and liquidus temperatures of the alloys were measured using DTA and the melting behavior for S-contents of 0 at%, 1 at%, 3 at %, 5 at% and 7 at% is shown in Fig. 1c). The S-free glass as well as the lower sulfur additions shows melting behavior that appears to be closely related to that of eutectic melting while at higher sulfur contents a pronounced "melting shoulder" with significantly higher T_l appears. A sulfur addition of 2 at% leads to the lowest liquidus temperature measured for the whole set, while the analyzed course of T_s and T_l mimics a eutectic behavior for the $(Zr_{50}Ti_{16.6}Ni_{18.3}Cu_{15})_{100-x}S_x$ system. Furthermore, the main peak of the melting event starts splitting into two separate melting peaks for higher sulfur additions. This indicates that the system deviates from eutectic behavior and sulfur induces a shift into a multiphase region. The derived solidus and liquidus temperature values and the reduced glass transition temperature $T_{rg} = (T_g/T_l)$ for sulfur additions from 0 at% to 8 at% are shown in Fig. 1d), where an initial decrease of the liquidus temperature upon sulfur introduction into the system can be seen with the lowest value of T_l being located at 2 at% of sulfur. While the alloy containing 3 at% S shows a lower T_l than the alloy without S, further increase of the S content results in an increasing liquidus temperature from 1.098 K at 2 at% sulfur to 1.218 K at 8 at% of sulfur. The solidus temperature stays rather constant over the course of the sulfur addition into the alloy except for a rise in solidus temperature at 8 at% S. The characteristic values for the whole range of sulfur additions are shown in Table 1 for a heating rate of 20 K/min.

3.2. X-ray diffraction

The introduction of sulfur into the system yielded several suitable alloys that were successfully cast into an amorphous structure with a sulfur addition in the range from 0 at% to 8 at%. The 0.25 mm thick plates were found to be X-ray amorphous throughout the whole range of sulfur that was added to the alloy. Subsequently the thickness of the casting was increased to 0.5 mm plates and 0.75 mm plates. Following experiments continued with 2 mm rods, where the amorphous structure was confirmed for a range of 1–6 at%. The upper limit of GFA was determined by consecutive casting and XRD analysis of 5 mm, 6 mm and 7 mm rod specimens for the relevant sulfur contents; the resulting spectra are shown in Fig. 2a) for the 6 mm rods and in Fig. 2b) for the crystalline 7 mm rods. While the 6 mm thick rods were X-ray amorphous for 2–3 at% S, for the 7 mm rods, no fully amorphous sample could be obtained, marking the 6 mm thickness as critical casting thickness for the $(Zr_{50}Ti_{16.6}Ni_{18.3}Cu_{15})S_2$ and $(Zr_{50}Ti_{16.6}Ni_{18.3}Cu_{15})S_3$ ($Zr_{50}S_3$) BMGs. A tendency of an increased proportion of amorphous phase towards the sulfur rich side can be seen for the 7 mm thick rods by noting the amorphous halo of the superposed spectrum of the $Zr_{50}S_3$ glass in contrast to the 2 at% containing variant. The summary presenting the results of consecutive casting and X-ray structural analysis are displayed in Fig. 2c). Furthermore, a casting series of 5 mm diameter rods was analyzed using synchrotron X-rays. The corresponding diffraction image and integrated spectrum for the $Zr_{50}S_3$ alloy Fig. 2d), where no traces of Bragg reflexes can be observed. Bragg reflexes would signify a relevant proportion of crystalline material within the sample which is not the case for the 5 mm rod of $Zr_{50}S_3$ confirming its fully amorphous structure. Therefore, the alloy $Zr_{50}S_3$ was determined to be the most promising alloy of the sulfur variation study. For the 6 mm rod a more detailed investigation of the local microstructure can be seen in Figure S2, under the high magnification of the TEM singular nanocrystals of about 20 nm size can be detected, which indicate the limit of the glass forming ability.

The plate specimens with a thickness of 0.75 mm as well as the cast 4 mm diameter rod specimens were further investigated by synchrotron X-ray diffraction and the resulting spectra of the 4 mm rods can be seen in Fig. 3a). A direct comparison of the resulting structure that can be found in Fig. 3b) and Fig. 3c). It is noteworthy that the crystalline phase formation that is encountered in the alloy variants without sulfur is inhibited/suppressed by the sulfur addition and the primary phase that forms upon solidification changes towards a different crystal structure, as shown in Fig. 3a). The structural data is compared with reference structures of the International Centre for Diffraction Data (ICDD) Powder Diffraction Files (PDF) database [26]. The cast 4 mm rods yield synchrotron X-ray amorphous samples with S-contents between 2 at% and 3 at%.

Table 1
Characteristic temperatures derived from the DSC and DTA measurements at a heating rate of 20 K/min, as well as the calculated values of the reduced glass transition temperature as a function of S-content (* marks values that were not determined due to overlapping of glass transition and early initial crystallization).

S (at%)	T_g^{onset} (K)	T_{x1} (K)	T_{x2} (K)	T_s (K)	T_l (K)	T_{rg}
0	*	*637*	*742*	*1072*	*1111*	
1	*	*655*	*748*	*1070*	*1108*	
2	*	*676*	*757*	*1069*	*1098*	
3	*640*	*686*	*765*	*1070*	*1105*	*0.587*
4	*659*	*706*	*781*	*1070*	*1135*	*0.581*
5	*677*	*726*	*793*	*1069*	*1154*	*0.579*
6	*689*	*754*	*794*	*1067*	*1171*	*0.575*
7	*699*	*774*		*1068*	*1193*	*0.574*
8	*713*	*778*		*1095*	*1218*	*0.574*

3.3. Influence of industrial grade material

The most promising alloy $Zr_{50}S_3$ was replicated from industrial grade Zr and Ti materials containing O that is inherent to the manufacturing process of the commercial Ti and Zr alloys. The quantification of the solvent oxygen content in the alloys was performed via carrier hot gas extraction in the laboratory of ChemiLytics GmbH. The results of the employed Zr grade R60702, the commercial purity grade 2 Ti as well as the final high purity alloy and the final industrial purity alloy of $Zr_{50}S_3$ are shown in Table 2. While high purity $Zr_{50}S_3$ contains 900 a-ppm O, the industrial grade alloy contains 4650 a-ppm O.

The same XRD tests that were performed on the high purity $Zr_{50}S_3$ alloys were conducted on the industrial grade materials. XRD results for 5 mm to 7 mm suction cast rods of the $Zr_{50}S_3$ alloy can be seen in Fig. 4a) indicating only a loss of 1 mm GFA due to the oxygen contamination. To show differences in material behavior with O contamination, Vitreloy 105 ($Zr_{52.5}Ti_5Ni_{14.6}Cu_{17.9}Al_{10}$) and AMZ4 ($Zr_{59.3}Cu_{28.8}Al_{10.4}Nb_{1.5}$) were reproduced with the same raw materials purity and casting method. The resulting XRD spectra of slices drawn from equivalent positions in the rods are shown for comparability for the AMZ4 alloy in Fig. 4b), reaching a GFA of only 3 mm and in Fig. 4c) for the Vit 105 alloy, reaching a GFA of only 4 mm. This underlines the impact of the industrial grade materials employed in the synthesis. Both alloys reach just half of the critical casting thickness found in the high purity variants, that can typically be cast into 8 mm rods [18] and still solidify fully amorphous, meaning a loss of 50 % of GFA in the industrial purity.

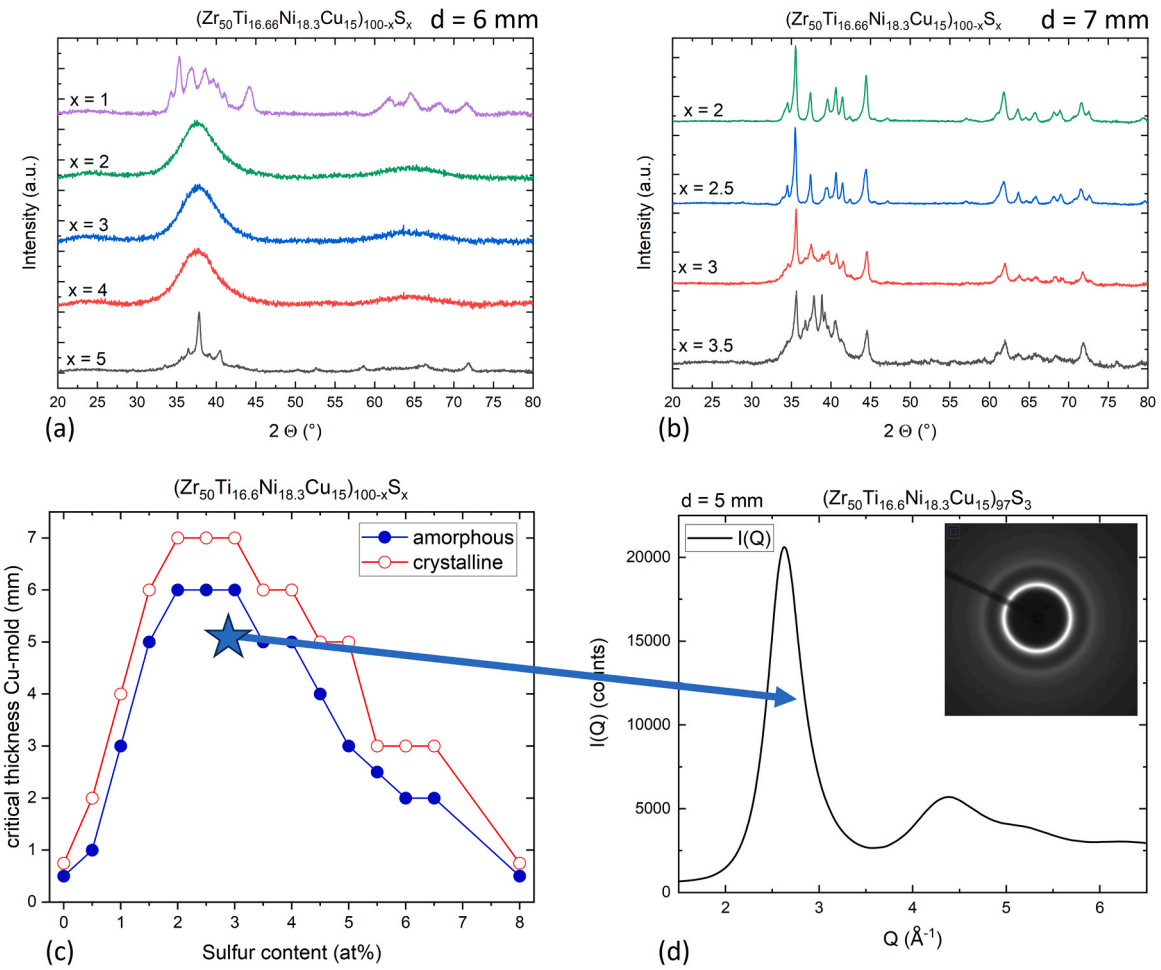

Fig. 2. a) Laboratory XRD results for the sulfur addition into the system from the series of alloys attributed with a glass forming ability of 6 mm b) XRD of the sulfur variation showing that the 7 mm rods surpass the critical thickness D_C. c) XRD data of samples with varying casting thickness as a function of S-content, and d) a synchrotron X-ray diffraction spectrum of a 5 mm rod that was produced from the $(Zr_{50}Ti_{16.6}Ni_{18.3}Cu_{15})_{97}S_3$ alloy by suction casting into water cooled copper molds.

3.4. Mechanical properties

For the $Zr_{50}S_3$ glass, 3-PBB and compression experiments were conducted to assess the strength and ductility for both the high purity and industrial variants. As shown in Fig. 5a), the high purity material exhibits a bending yield strength of 2.59 GPa with a fracture strain of 5.2 ± 0.29 %. The ultimate bending strength is close to 3 GPa which is well within the spectrum of expected maximum bending strengths for a Zr-based BMG. The industrial grade material results are displayed in Fig. 5b). The offset bending yield strength of 2.5 GPa is close to the high purity variant and, despite the much higher oxygen level, about 80 % of the high purity ductility was retained with a bending fracture strain of 4.18 ± 0.71 %.

The compressive testing results are shown in Fig. 5c) for the high purity alloy and d) for the industrial grade alloy, where once again the industrial purity variant performed well. For the high purity variant, the compressive strength was determined to be 1.65 GPa paired with a total strain to failure of 5.8 ± 0.6 % and for the industrial grade material, a slightly higher compressive strength of 1.72 GPa was determined with a slightly higher strain to failure value of 6.6 ± 0.3 %. The results show little scattering between the samples, embodied by the small standard deviation. An overview of the bending and compression data is given in Table 3.

Load-displacement data from fracture toughness tests of the high purity and the industrial grade glasses are shown in Fig. 6a) and b), respectively. The conditional fracture toughness, K_Q, value that was derived from the experiments is 104.4 ± 6. 9 MPa$\sqrt{m}$ for the high purity variant of the glass and for the industrial grade variant K_Q is 79 ± 5.9 MPa$\sqrt{m}$, which is only a reduction of 24 %. The difference in K_J values between the two materials qualities is greater than the difference in K_Q values. The high purity variant shows a high K_J value of 159.5 ± 37.4 MPa$\sqrt{m}$ which indicates more significant plastic deformation compared to the industrial quality alloy that achieves a significantly lower K_J value of 89.5 ± 9.5 MPa$\sqrt{m}$.

Additionally, microhardness mapping with HV0.05 indents was performed on both variants of the $Zr_{50}S_3$ alloy. The hardness maps with a lateral resolution of 40 μm can be seen in Fig. 6c) for the high purity as well as in Fig. 6d) for the industrial grade variant, respectively. The average HV0.05 hardness value increases from 512.4 ± 3.1 HV0.05 in the high purity variant to 528 ± 3.6 HV0.05 in the industrial variant due to the 828 w-ppm (3750 a-ppm) increase in oxygen content in the metallic glass. While the distribution of hardness depicts an average hardness that is located between 515 and 525 HV0.05 (embodied by a mostly light green area) with distinct soft spots that show a hardness below 510 HV0.05 in the hardness map. The industrial grade material shows an inverted behavior, here the main part of the distribution of the hardness values falls into the 520–530 HV0.05 range with distinct hard spots of up to 540 HV0.05. Microhardness was also probed as a function of the S-content using higher load Vickers hardness (HV5) experiments and the results can be seen in Fig. 6e) where the HV5 values are displayed as a function of the added S. The hardness starts at about 480 HV5 for the 1 at% addition of sulfur and rises with S to about 580 HV5

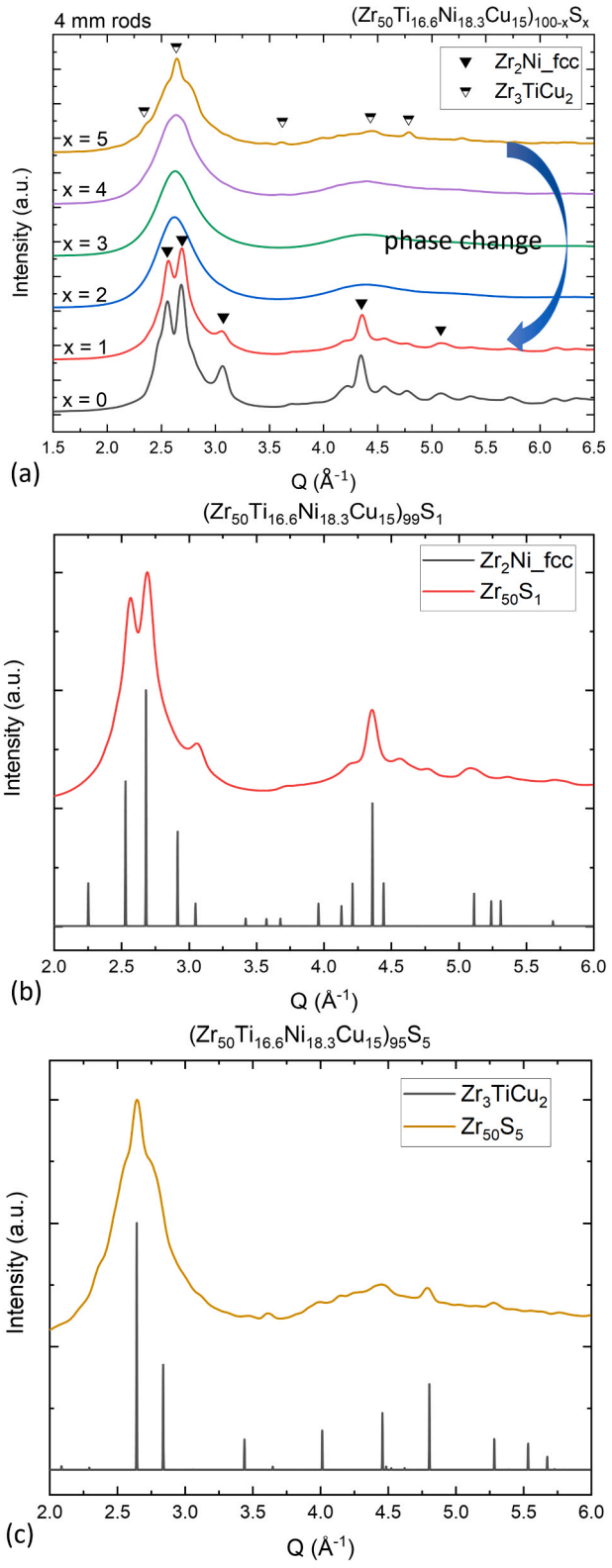

Fig. 3. a) Synchrotron diffraction spectra of 4 mm diameter suction cast rods ranging from 0 at% to 5 at% S. Synchrotron diffraction spectra for 4 mm diameter rod specimens with b) 1 at% S and c) 5 at% S with direct comparisons to the PDF reference structural data. The difference in crystalline primary phase is emphasized by the individual comparison and indicated. The system changes due to the sulfur impact from a primary fcc-type Zr_2Ni phase (ref. PDF 00–041–0898) to an intermetallic compound type $(Zr_3Ti)(NiCu)$ phase (ref. PDF 01–079–3665).

Table 2
Determined oxygen contents for the cast alloys as well as the commercial purity alloys employed in their synthesis.

material	oxygen (w-ppm)	oxygen (a-ppm)
Zr R60702	1368	7750
Ti cp grade 2	1639	4880
$(Zr_{50}Ti_{16.6}Ni_{15}Cu_{18.3})S_3$ high purity	198	900
$(Zr_{50}Ti_{16.6}Ni_{15}Cu_{18.3})S_3$ industrial	1026	4650

with 6 at% S.

4. Discussion

Sulfur bearing BMG alloys were discovered only recently and have been reported to have a good resistance towards oxygen contamination as they could be replicated from industrial grade material without great GFA loss [14]. The previously reported $Ti_{40}Zr_{35}Cu_{17}S_8$ and $Zr_{56}Ti_{13.3}Ni_{13.6}Cu_{9.6}S_7$ alloys fulfill those requirements; however, the GFA is quite limited in the case of the Zr-rich $Zr_{56}Ti_{13.3}Ni_{13.6}Cu_{9.6}S_7$ alloy as it can only reach about 1 mm of casting thickness. The $Zr_{50}Ti_{16.6}Ni_{18.3}Cu_{15}$ alloy possesses a reported GFA of 1 mm without sulfur and was therefore chosen for the introduction of sulfur into the system with the goal of developing an oxygen tolerant Zr-Ti-Ni-Cu-S alloy with good mechanical properties and improved GFA. Sulfur possesses a negative enthalpy of mixing for the constituents of the Zr-Ti-Ni-Cu system and quickly forms sulfide compounds as the solubility of sulfur in the intermetallic phases and the regular crystalline phases is low [27]. This behavior is quite similar to other metalloid additions to BMG forming alloy systems like P or Si. For the liquid phase of the Zr-Ti-Ni-Cu-S, however, this is different as all binary phase diagrams of the Ti-Zr-Ni-Cu-S system contain areas with a homogeneous liquid phase, where all sulfur is in solution within the liquid phase, similar to the case of the phase diagram of the Ti-S system [28]. Sulfur has a small atomic radius of 102 pm compared to Ni (125 pm) and Cu (128 pm) as well as Ti (146 pm) and Zr (161 pm) [29]. The mismatch in atomic size and the negative heat of mixing of the constituents are known to improve the GFA according to the empirical rules proposed by Inoue [30,31]. The mismatch in atomic size can be expressed by the δ parameter that was calculated according to reference [32] with the atomic radii mentioned before. The base alloy already shows a high δ value typical for intermetallic alloys and δ rises further with progressing S-addition, a comparison with GFA and characteristic temperatures can be seen in Figure S3. A direct correlation between the δ and GFA or the change in characteristic temperatures cannot be determined. This is likely due to the chemical contribution of the S to the alloys behavior, for the liquid of the similar Ti-Ni-S system Wilden et al. reported “that Sulfur may occupy a larger space in the melt structure than the one assumed for hard spheres with covalent radii” [33]. Therefore, we conclude that the effect of S on GFA and SCLR cannot be interpreted accurately by a topological model of hard spheres alone in this alloy system.

As more S is added, however, the alloy is positioned closer to the stochiometric sulfide compounds whose formation rivals the glass-formation during cooling from the liquid state. Those opposing effects of S additions are likely to create an optimum for the S addition in terms of GFA, where the balance between those effects is reached. For the $Zr_{50}Ti_{16.6}Ni_{18.3}Cu_{15}$ alloy, the maximum GFA is reached at 3 at% of sulfur addition. The combination of a lower T_l and suppressed regular crystallization pathway by adequate sulfur addition enables the high GFA for this alloy. From this point on, any further sulfur addition leads to a steep increase in T_l which reduces T_{rg}. The onset of the glass transition, T_g^{onset}, shifts to higher temperatures with increasing sulfur content and a similar, yet steeper, increase in crystallization temperature T_{x1} is measured to give an enhanced SCLR. The maximum in GFA and SCLR size do not align as the GFA of the 7 at% sulfur addition is only up to 1 mm while the SCLR region of the 3 at% sulfur addition is not

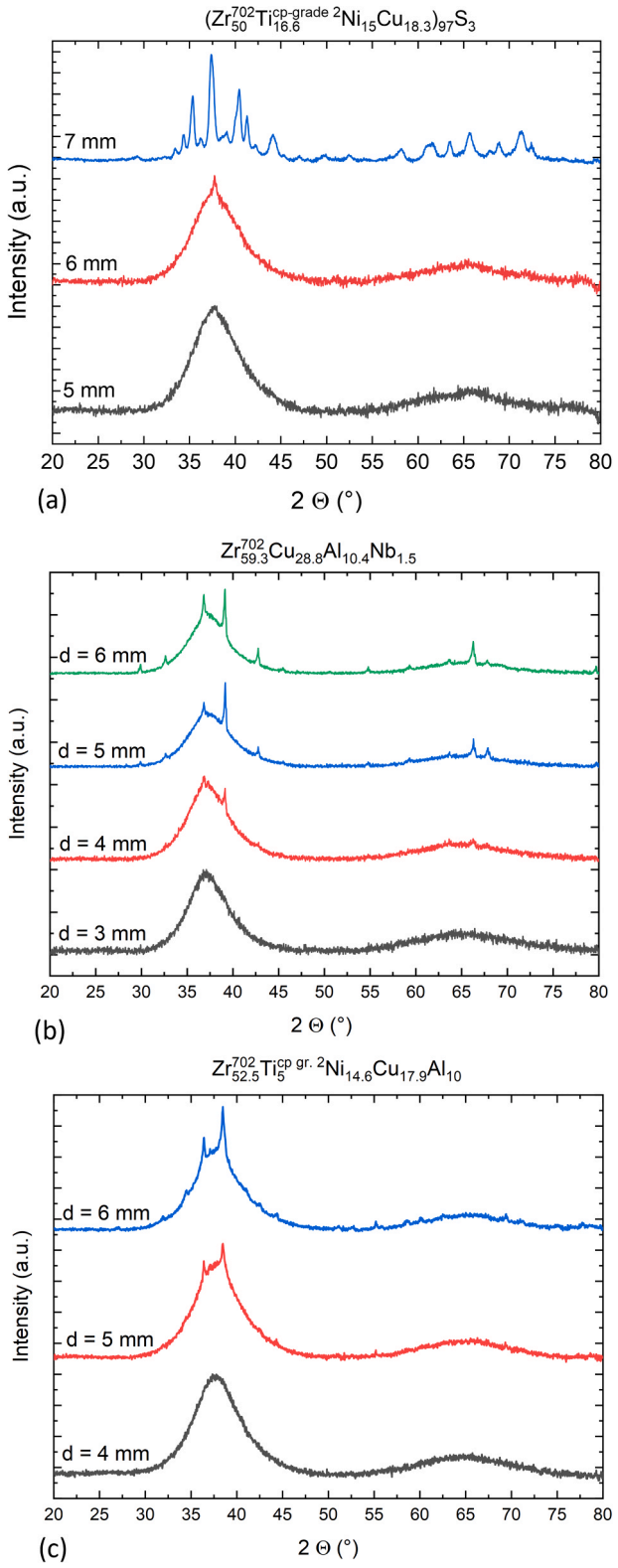

Fig. 4. a) XRD results of industrial grade material for the best found alloy $(Zr_{50}Ti_{16.6}Ni_{18.3}Cu_{15})_{97}S_3$ of diameter 5 mm to diameter 7 mm suction cast rod specimen b) XRD results of diameter 3 mm to diameter 6 mm suction cast rods of the industrial grade material AMZ4 alloy showing no spectrum that signifies fully amorphous structure beyond the 3 mm diameter casting thickness c) XRD spectrum of rods with diameters 4 mm to 6 mm of Vit105 alloy synthesized from the same industrial grade materials.

pronounced.

The sulfur induced a different precipitate phase that is characterized by its independence from the amount of oxygen contamination in the alloy, as the dominant non-metallic component is the sulfur in the alloy's composition. Sulfur was found to promote intermetallic crystallization over icosahedral crystallization and following intermetallic crystallizations from the SCLR as well as during casting processes in previous studies [16,34]. This change in primary crystal phase can also be responsible for a significant improve the mechanical properties as Ruschel et al. discovered when correlating SCLR crystallization behavior and mechanical properties of the amorphous phase in the Ti-Zr-Ni-Cu-S system [16]. Therefore, in the Zr-Ti-Ni-Cu-S system there might result an analogous situation. Sulfur induces two different effects related to the mechanical properties. It increases the hardness which is accompanied by an embrittlement. On the other hand, it reduces the influence of oxygen load on the mechanical properties by altering the primary phase. The addition of 3 at% of sulfur into the alloy was found to be a profound balance between those opposing effects.

The influence of oxygen on the crystallization of bulk glass forming systems has been investigated thoroughly in previous studies, especially for Zr-based systems. As Gebert et al. described for the Zr-Cu-Ni-Al system, oxygen induces the crystallization of a metastable fcc $NiZr_2$ type phase that then serves as heterogeneous nucleation site for the intermetallic compound crystallization [35]. For S-infused alloys, the previously reported effect of a changed primary crystallization [34] and the resulting stalling of the following intermetallic crystallization are likely responsible for this positive influence on the GFA under high oxygen load analogous to the sulfur additions in the Ti-Zr-Cu system [14]. The alloy $(Zr_{50}Ti_{16.6}Ni_{15}Cu_{18.3})_{97}S_3$ shows indeed good tolerance against higher levels of O contamination with the alloy losing only 1 mm of critical casting thickness when processed from low purity industrial grade material. This confirms the previous findings of Kuball et al. regarding the oxygen resilience of sulfur bearing BMGs. Compared to the reference material Vit105, the decrease in GFA by oxygen contamination is significantly smaller, as Vit105 usually reaches a GFA of up to 8 mm in copper mold casting and drops to 4 mm GFA with 1000 w-ppm of oxygen that results from using Zr-R60702 and Ti grade 2 [18].

For amorphous Cu-Zr-S Jiang et al. reported Zr-S cluster in the amorphous phase, it is reasonable that similar cluster are encountered in this system [36]. The chemical similarity between oxygen and sulfur, as well as the existence of the sulfuric precipitates, insinuates that instead of forming oxide phases, which are detrimental towards the GFA, the oxygen atoms could be integrated substitutionally into Zr-S clusters. These would then rather tend to form the earlier reported less detrimental sulfide phases as primary phase, interfering with the glass formation instead of the more detrimental oxides like Zr_4Cu_2O during solidification from the melt [34].

While the bending ductility and fracture toughness of the industrial grade variant were reduced by ~20 – 25 % compared to that of the high purity variant, the yield strength and compressive ductility were slightly enhanced. Both high purity and industrial grade compressive strength values are within the range of typical values for Zr-BMG, i.e., 1.6–1.8 GPa [37] – depending on the sample size and composition of the Zr-BMG. The compressive strength however is remarkable in the case of the industrial grade variant as the high content of oxygen does not trigger oxide particle crystallization that leads to a decrease in mechanical strength as in the case of the Vitreloy 106 alloy reported by Conner et al., where a contamination of 960 w-ppm lead to a loss of 420 MPa of compressive strength in 3 mm diameter samples [38]. Thus, the mechanical performance of the $(Zr_{50}Ti_{16.6}Ni_{15}Cu_{18.3})_{97}S_3$ alloy is much better than expected based on the numerous publications on the detrimental effect of both solvent oxygen and oxides on the mechanical properties of Zr-based BMGs [12,38–40]. Overall, the ductility and fracture toughness of the $(Zr_{50}Ti_{16.6}Ni_{15}Cu_{18.3})_{97}S_3$ alloy appear to be sufficient for engineering applications even in the industrial grade variant.

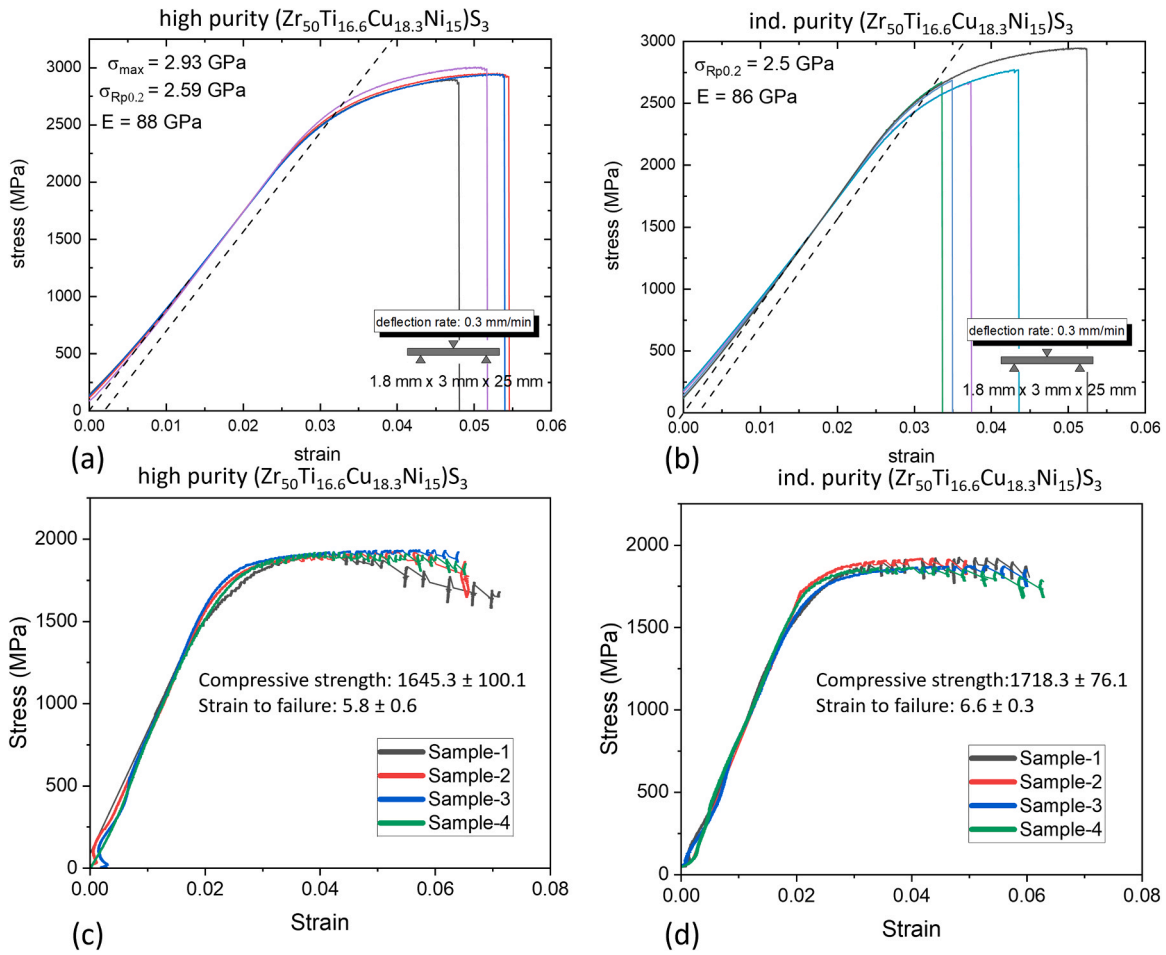

Fig. 5. a) 3-PBB stress strain curves showing an engineering bending strength of 2.59 GPa paired with a bending elongation limit that lies consistently above 4.5 %. b) 3PBB stress strain curves of the industrial grade material, and c) compressive testing results for the high purity variant of the alloy. d) Compressive testing results for the industrial grade alloy.

Table 3
Determined characteristic mechanical properties for the high purity and industrial grade variant of the amorphous $(Zr_{50}Ti_{16.6}Ni_{15}Cu_{18.3})_{97}S_3$ alloy, listed are the maximum yield stresses σ_{max}, the offset yield strength $\sigma_{0.2}$ the breaking elongation ε_{break} and the standard deviation SD.

3-PBB	σ_{max}	SD	$\sigma_{0.2}$	SD	ε_{break}	SD
	[MPa]	[MPa]	[MPa]	[MPa]	[%]	[%]
high purity	2932	25	2598	22	5.20	0.29
industrial	2745	112	2518	84	4.18	0.71
compr.	σ_{max}	SD	ε_{break}	SD		
	[MPa]	[MPa]	[%]	[%]		
high purity	1645	100.1	5.8	0.6		
industrial	1718	76	6.6	0.3		
hardness	HV0.05	SD				
high purity	512.4	3.1				
industrial	528.6	3.6				

Next, embrittlement due to precipitation of Zr_4Cu_2O and Zr_4Ni_2O oxide phases does not seem to occur in sulfur containing alloys. In a previous study of the Ti-Zr-Cu-S system we observed a change in primary crystallization from Zr_2(Cu, Ni) intermetallic compounds to sulfuric Zr-Ti-S precipitates that precede the intermetallic crystallization, which ensued heterogeneously on the surface of the sulfuric precipitates [34]. Here the difference in crystallization mechanism due to the presence of sulfur becomes relevant for the mechanical properties, too, yet the alloys plasticity is only slightly reduced in 3-PBB while during compressive testing, no deterioration of plasticity was observed for the industrial alloy despite a high load of oxygen.

The hardness maps show the influence of the oxygen on the distribution of soft "spots" within the harder matrix phase in the high purity variant. For the industrial grade variant, this relation is encountered inversely: the spots are harder than the softer matrix phase. The existence of relatively soft regions in Zr-based and Ni-based BMGs has been associated with larger medium range order (MRO) clusters that are thought to act as shear transition zone (STZ) nuclei [25,41,42]. Furthermore, the relatively softer microstructure is thought to promote the higher ductility and fracture toughness of the high purity material over the industrial material. Hardness testing reveals a near linear increase in Vickers hardness depending on the sulfur content with a maximum of 580 HV5 at 6 at% sulfur that is associated with an embrittlement of the amorphous phase, similar to the effect of O in Zr-based BMGs. The embrittlement effect of S, however, seems to be less pronounced than that of oxygen as BMGs with oxygen content above 1 at% addition have been reported to be near-ideal brittle, like in the case of Vit106 [38], while the sulfur containing BMGs in this study retain significant ductility.

5. Conclusion

In conclusion the study can be summarized with the main findings listed below:

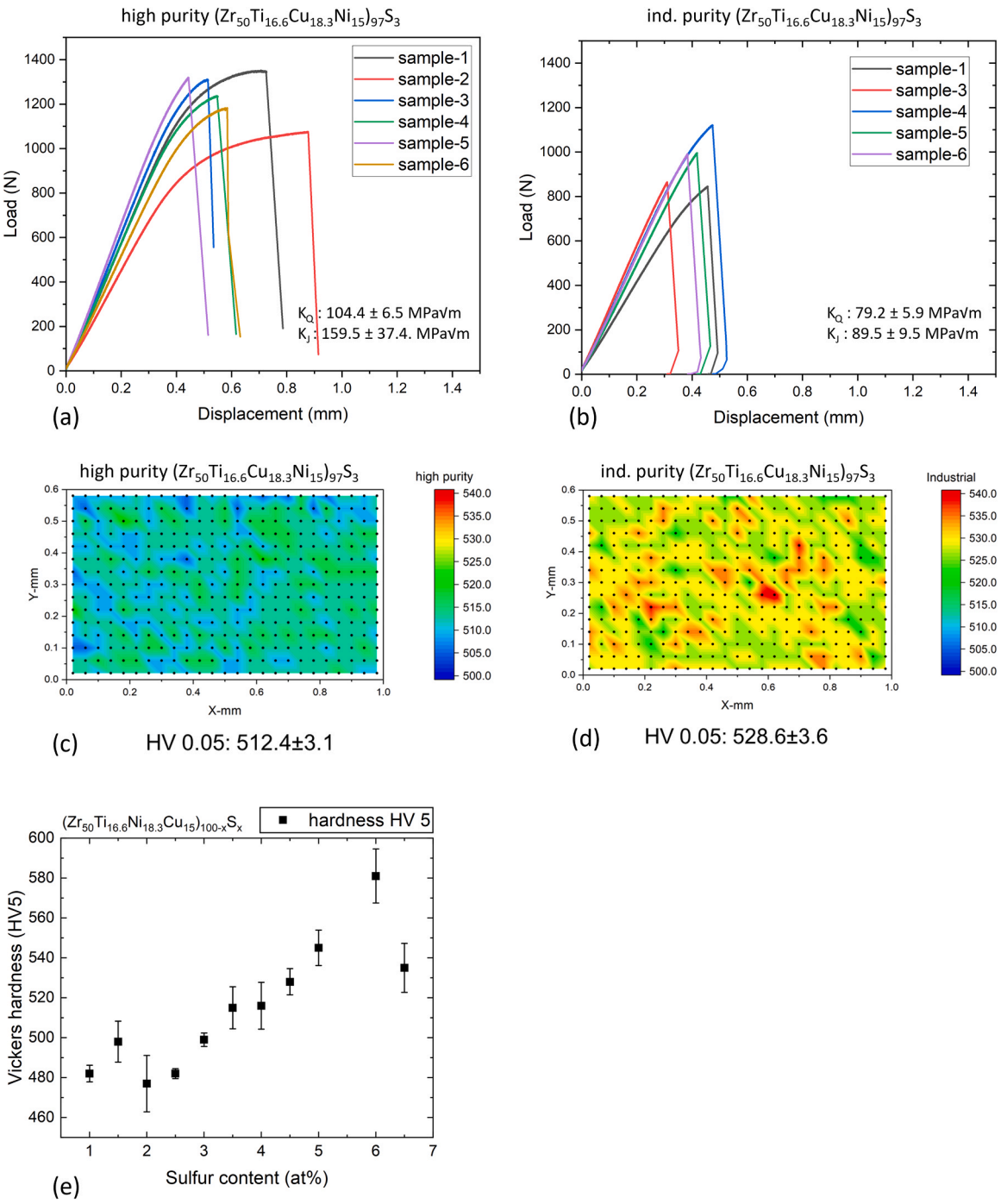

Fig. 6. Fracture toughness testing results for SEN(B) samples tested in 3-point bending for a) the high purity variant of the $Zr_{50}S_3$ and b) the industrial grade purity variant of the alloy $Zr_{50}S_3$ c) microhardness maps HV0.05 of the high purity variant and d) microhardness map of the industrial grade variant of the alloy, showing a significant higher average hardness than the high purity variant of the alloy, and e) determined Vickers hardness HV5, depending on the sulfur content in the alloy $(Zr_{50}Ti_{16.6}Ni_{18.3}Cu_{15})_{100-x}S_x$ showing a rise in hardness of 100 HV5 from 1 at% to 6 at% of sulfur.

- The introduction of sulfur is found to be beneficial for both GFA at 3 at% of sulfur and SCLR stability at 7 at% of sulfur, although these properties are maximized at different sulfur contents.
- The reduction of the GFA due to a high oxygen load of 4650 a-ppm oxygen from using industrial grade starting materials is less than 20 %.
- The developed alloys show excellent yield strength, compressive ductility and fracture toughness that can be retained to a high degree under the oxygen load of industrial grade purity.
- Overall, the system is found to be a promising candidate for developing lower cost BMGs produced from industrial purity elements that will be more attractive for various engineering applications compared to high purity BMGs.

The authors find in this system a very promising candidate to further investigate the beneficial effect of sulfur, especially the steep rise in glass forming ability from 0.25 mm to 6 mm glass forming due to 3 at% of sulfur sparks the question of its influence on viscosity and thermodynamic properties of the melt. Further studies of this system will target in

depth those questions as well as analyze the alterations of the structure in the liquid and amorphous phase due to the sulfur's presence.

CRediT authorship contribution statement

Busch Ralf: Writing – review & editing, Supervision, Project administration, Funding acquisition, Conceptualization. **Adam Bastian:** Writing – review & editing, Writing – original draft, Visualization, Investigation, Formal analysis, Conceptualization. **Kruse Oliver:** Visualization, Investigation. **Jiang Hao-Ran:** Writing – review & editing, Investigation. **Li Bosong:** Writing – review & editing, Methodology, Investigation. **Gludovatz Bernd:** Writing – review & editing, Supervision, Methodology, Conceptualization. **Kruzic Jamie J.:** Writing – review & editing, Supervision, Project administration, Methodology, Funding acquisition, Conceptualization. **Ruschel Lucas Matthias:** Writing – review & editing, Methodology, Investigation, Conceptualization. **Neuber Nico:** Writing – review & editing, Investigation. **Frey Maximillian:** Writing – review & editing, Investigation. **Gross Oliver:** Writing – review & editing, Resources, Investigation.

Declaration of Competing Interest

The authors declare the following financial interests/personal relationships which may be considered as potential competing interests: Bastian Adam reports was provided by Saarland University Chair of Metallic Materials. If there are other authors, they declare that they have no known competing financial interests or personal relationships that could have appeared to influence the work reported in this paper.

Acknowledgements

Instrumentation and technical assistance for this work were provided by the Service Center X-ray Diffraction, with financial support from Saarland University and German Science Foundation (project number INST 256/349–1). The authors thank Dr. Oliver Janka for the support in collection of the conventional X-ray diffraction data presented in this paper. Additional financial support was provided by the Australian Research Council (grant number DP240101127) and JJK thanks the Alexander von Humboldt Foundation for their support through the Friedrich Wilhelm Bessel Research Award. The authors also thank the Heraeus AMLOY Technologies GmbH for providing the high-quality raw materials employed in the synthesis of the alloys for this work. The authors acknowledge the DESY (Hamburg, Germany), a member of the Helmholtz Association HGF and give our thanks to Dr. Soham Banerjee and Dr. Ann-Christin Dippel for the experimental support and operation of the P21.1 beamline facility during the HE-XRD experiments. The work made use of the resources of the Correlative Microscopy and Tomography (CoMiTo) core facility at Saarland University. The authors thank Christoph Pauly of the core facility CoMiTo, Saarland University, for carrying out the measurement. Funding for TEM by the European Union via the European Regional Development Fund (ERDF) as part of the operational programme EFRE Saarland 2014–2020 under the objective "Investitionen in Wachstum und Beschäftigung" is gratefully acknowledged.

Appendix A. Supporting information

Supplementary data associated with this article can be found in the online version at doi:10.1016/j.jallcom.2025.180307.

References

[1] J.J. Kruzic, Bulk metallic glasses as structural materials: a review, Adv. Eng. Mater. 18 (2016) 1308–1331, https://doi.org/10.1002/adem.201600066.
[2] A. Peker, W.L. Johnson, A highly processable metallic glass: Zr41.2Ti 13.8Cu12.5Ni10.0Be22.5, Appl. Phys. Lett. 63 (1993) 2342–2344, https://doi.org/10.1063/1.110520.
[3] D. Wang, Y. Li, B.B. Sun, M.L. Sui, K. Lu, E. Ma, Bulk metallic glass formation in the binary Cu-Zr system, Appl. Phys. Lett. 84 (2004) 4029–4031, https://doi.org/10.1063/1.1751219.
[4] T. Zhang, A. Inoue, T. Masumoto, Amorphous Zr-Al-TM (TM=Co, Ni, Cu) alloys with significant supercooled liquid region of over 100 K, Mater. Trans. JIM 32 (1991) 1005–1010, https://doi.org/10.2320/matertrans1989.32.1005.
[5] X.H. Lin, W.L. Johnson, Formation of Ti–Zr–Cu–Ni bulk metallic glasses, J. Appl. Phys. 78 (1995) 6514–6519, https://doi.org/10.1063/1.360537.
[6] X.H. Lin, W.L. Johnson, W.K. Rhim, Effect of oxygen impurity on crystallization of an undercooled bulk glass forming Zr-Ti-Cu-Ni-Al alloy, Mater. Trans. JIM 38 (1997) 473–477, https://doi.org/10.2320/matertrans1989.38.473.
[7] S.E. Naleway, R.B. Greene, B. Gludovatz, N.K.N. Dave, R.O. Ritchie, J.J. Kruzic, A highly fatigue-resistant Zr-based bulk metallic glass, Metall. Mater. Trans. A Phys. Metall. Mater. Sci. 44 (2013) 5688–5693, https://doi.org/10.1007/s11661-013-1923-4.
[8] J. Heinrich, R. Busch, B. Nonnenmacher, Processing of a bulk metallic glass forming alloy based on industrial grade Zr, Intermetallics 25 (2012) 1–4, https://doi.org/10.1016/j.intermet.2012.02.011.
[9] L.M. Ruschel, S. Jakovlev, O. Gross, N. Neuber, B. Adam, M. Frey, B. Schmidt, B. Bochtler, R. Busch, Unraveling the role of relaxation and rejuvenation on the structure and deformation behavior of the Zr-based bulk metallic glass Vit105, Mater. Today Adv. 23 (2024) 100522, https://doi.org/10.1016/j.mtadv.2024.100522.
[10] P.J. Tao, Y.Z. Yang, X.J. Bai, Z.W. Xie, X.C. Chen, Z.J. Dong, J.G. Wen, H.J. Long, Zr-based bulk metallic glass with super-plasticity under uniaxial compression at room temperature, J. Non Cryst. Solids 354 (2008) 3742–3746, https://doi.org/10.1016/j.jnoncrysol.2008.04.012.
[11] C.T. Liu, M.F. Chisholm, M.K. Miller, Oxygen impurity and microalloying effect in a Zr-based bulk metallic glass alloy, Intermetallics 10 (2002) 1105–1112, https://doi.org/10.1016/S0966-9795(02)00131-0.
[12] C.A. Teixeira, R.V. da Silva, L.T. Pereira, M.F. de Oliveira, Oxygen effect on bending behavior of a zirconium based bulk metallic glass, J. Non Cryst. Solids 535 (2020), https://doi.org/10.1016/j.jnoncrysol.2020.119966.
[13] A. Kuball, B. Bochtler, O. Gross, V. Pacheco, M. Stolpe, S. Hechler, R. Busch, On the bulk glass formation in the ternary Pd-Ni-S system, Acta Mater. 158 (2018) 13–22, https://doi.org/10.1016/j.actamat.2018.07.039.
[14] A. Kuball, O. Gross, B. Bochtler, B. Adam, L. Ruschel, M. Zamanzade, R. Busch, Development and characterization of titanium-based bulk metallic glasses, J. Alloy. Compd. 790 (2019) 337–346, https://doi.org/10.1016/j.jallcom.2019.03.001.
[15] A. Kuball, Development, Characterization and Processing of a Novel Family of Bulk Metallic Glasses: Sulfur-Containing Bulk Metallic Glasses, University of Saarland, 2019.
[16] L.M. Ruschel, B. Adam, O. Gross, N. Neuber, M. Frey, H.J. Wachter, R. Busch, Development and optimization of novel sulfur-containing Ti-based bulk metallic glasses and the correlation between primarily crystallizing phases, thermal stability and mechanical properties, J. Alloy. Compd. 960 (2023) 170614, https://doi.org/10.1016/j.jallcom.2023.170614.
[17] O. Gross, L. Ruschel, A. Kuball, B. Bochtler, B. Adam, R. Busch, Bulk metallic glass formation in the (Ti,Zr)–(Ni,Cu)–S system, J. Phys. Condens. Matter 32 (2020) 264003, https://doi.org/10.1088/1361-648X/ab7c15.
[18] B. Bochtler, Thermophysical and structural investigations of a CuTi- and a Zr-based bulk metallic glass, the influence of minor additions, and the relation to thermoplastic forming, 2019,https://doi.org/https://doi.org/10.22028/D291-31111.
[19] N. Grund, D. Holland-Moritz, S. Khademorezaian, L.P. Kreuzer, N. Neuber, L. M. Ruschel, H. Voigt, J. Wilden, F. Yang, S. Banerjee, M. Blankenburg, A.-C. Dippel, J.P. Embs, S. Divinski, R. Busch, A. Meyer, G. Wilde, Impact of sulfur addition on the structure and dynamics of Ni–Nb alloy melts, APL Mater. 12 (2024), https://doi.org/10.1063/5.0205058.
[20] H.-R. Jiang, J.-Y. Hu, N. Neuber, B. Bochtler, B. Adam, S.S. Riegler, M. Frey, L. Ruschel, W.-F. Lu, A.-H. Feng, R. Busch, J. Shen, Effect of sulfur on the glass-forming ability, phase transformation, and thermal stability of Cu-Zr-Al bulk metallic glass, Acta Mater. 212 (2021) 116923, https://doi.org/10.1016/j.actamat.2021.116923.
[21] V.V. Molokanov, V.N. Chebotnikov, Glass forming ability, structure and properties of Ti and Zr-intermetallic compound based alloys, Key Eng. Mater. (1990) 319–331, https://doi.org/10.4028/www.scientific.net/kem.40-41.319.
[22] V.V. Molokanov, M.I. Petrzhik, T.N. Mikhailova, T.A. Sviridova, N.P. Djakonova, Formation of bulk (Zr, Ti)-based metallic glasses, J. Non Cryst. Solids 250-252 (1999) 560–565, https://doi.org/10.1016/S0022-3093(99)00132-5.
[23] G. Ashiotis, A. Deschildre, Z. Nawaz, J.P. Wright, D. Karkoulis, F.E. Picca, J. Kieffer, The fast azimuthal integration Python library: pyFAI, J. Appl. Crystallogr 48 (2015) 510–519, https://doi.org/10.1107/S1600576715004306.
[24] X. Qiu, J.W. Thompson, S.J.L. Billinge, PDFgetX2: a GUI-driven program to obtain the pair distribution function from X-ray powder diffraction data, 678–678, J. Appl. Crystallogr 37 (2004), https://doi.org/10.1107/S0021889804011744.
[25] B. Li, L.M. Ruschel, K. Nomoto, O. Gross, B. Adam, N. Neuber, M. Frey, S.P. Ringer, B. Gludovatz, R. Busch, J.J. Kruzic, Fracture behavior of NiNb and NiNbP bulk metallic glasses, J. Alloy. Compd. 1010 (2025) 177369, https://doi.org/10.1016/j.jallcom.2024.177369.
[26] S. Gates-Rector, T. Blanton, The powder diffraction file: a quality materials characterization database, Powder Diffr. 34 (2019) 352–360, https://doi.org/10.1017/S0885715619000812.
[27] H. Wada, K. Takada, T. Sasaki, DSC studies on reactions of the elements with sulfur, Solid State Ion. 172 (2004) 421–424, https://doi.org/10.1016/j.ssi.2004.03.027.

[28] K. Hirata, S. Iikubo, H. Fujimoto, H. Ohtani, Thermodynamic assessment of Fe–Ti–S ternary phase diagram, Calphad 57 (2017) 62–77, https://doi.org/10.1016/J.CALPHAD.2017.02.006.
[29] K.J. Laws, D.B. Miracle, M. Ferry, Supplementary Materials – a predictive structural model for bulk metallic glasses, Nat. Commun. 6 (2015) 8123. ⟨http://www.nature.com/doifinder/10.1038/ncomms9123⟩.
[30] A. INOUE, Stabilization of supercooled liquid and opening-up of bulk glassy alloys, Proc. Jpn. Acad. Ser. B 73 (1997) 19–24, https://doi.org/10.2183/pjab.73.19.
[31] A. Inoue, Stabilization of metallic supercooled liquid and bulk amorphous alloys, Acta Mater. 48 (2000) 279–306, https://doi.org/10.1016/S1359-6454(99)00300-6.
[32] Y. Wu, P.K. Liaw, R. Li, W. Zhang, G. Geng, X. Yan, G. Liu, Y. Zhang, Relationship between the unique microstructures and behaviors of high-entropy alloys, Int. J. Miner. Metall. Mater. 31 (2024) 1350–1363, https://doi.org/10.1007/s12613-023-2777-4.
[33] J. Wilden, F. Yang, D. Holland-Moritz, S. Szabó, W. Lohstroh, B. Bochtler, R. Busch, A. Meyer, Impact of sulfur on the melt dynamics of glass forming Ti75Ni25-xSx, Appl. Phys. Lett. 117 (2020), https://doi.org/10.1063/5.0012409.
[34] B. Adam, A. Kuball, L.M. Ruschel, N. Neuber, M. Frey, R. Busch, Sulphuric precipitates in novel titanium-based, sulphur-bearing bulk metallic glass – a BMG composite? Philos. Mag. Lett. 104 (2024) 1–11, https://doi.org/10.1080/09500839.2024.2376614.
[35] A. Gebert, J. Eckert, L. Schultz, Effect of oxygen on phase formation and thermal stability of slowly cooled Zr65Al7.5Cu17.5Ni10 metallic glass, Acta Mater. 46 (1998) 5475–5482, https://doi.org/10.1016/S1359-6454(98)00187-6.
[36] H.-R. Jiang, J.-Y. Hu, N. Neuber, M. Frey, L. Xu, K. Sun, Y.-D. Jia, G. Wang, R. Busch, J. Shen, Influence of sulfur addition on the glass formation, phase transformation and mechanical properties of Cu50Zr50 alloy, Acta Mater. 255 (2023) 119064, https://doi.org/10.1016/j.actamat.2023.119064.
[37] T. Zhang, X. Meng, C. Wang, L. Li, J. Yang, W. Li, R. Li, Y. Zhang, Investigations of new bulk metallic glass alloys fabricated using a high-pressure die-casting method based on industrial grade Zr raw material, J. Alloy. Compd. 792 (2019) 851–859, https://doi.org/10.1016/j.jallcom.2019.03.357.
[38] R.D. Conner, R.E. Maire, W.L. Johnson, Effect of oxygen concentration upon the ductility of amorphous Zr57Nb5Al10Cu15.4 Ni12.6, Mater. Sci. Eng. A 419 (2006) 148–152, https://doi.org/10.1016/j.msea.2005.12.009.
[39] W.H. Zhou, F.H. Duan, Y.H. Meng, C.C. Zheng, H.M. Chen, A.G. Huang, Y.X. Wang, Y. Li, Effect of alloying oxygen on the microstructure and mechanical properties of Zr-based bulk metallic glass, Acta Mater. 220 (2021), https://doi.org/10.1016/j.actamat.2021.117345.
[40] I. Jonas, W. Hembree, F. Yang, R. Busch, A. Meyer, Industrial grade versus scientific pure: Influence on melt properties, Appl. Phys. Lett. 112 (2018) 1–5, https://doi.org/10.1063/1.5021764.
[41] K. Nomoto, A.V. Ceguerra, C. Gammer, B. Li, H. Bilal, A. Hohenwarter, B. Gludovatz, J. Eckert, S.P. Ringer, J.J. Kruzic, Medium-range order dictates local hardness in bulk metallic glasses, Mater. Today 44 (2021) 48–57, https://doi.org/10.1016/j.mattod.2020.10.032.
[42] B. Li, V. Yakubov, K. Nomoto, S.P. Ringer, B. Gludovatz, X. Li, J.J. Kruzic, Superior mechanical properties of a Zr-based bulk metallic glass via laser powder bed fusion process control, Acta Mater. 266 (2024) 119685, https://doi.org/10.1016/j.actamat.2024.119685.